Plasma Formation in Ambient Fluid from Hypervelocity Impacts

Shafquat T. Islam[1], Wentao Ma[1], John G. Michopoulos[2], and Kevin Wang*[1]

[1]Department of Aerospace and Ocean Engineering, Virginia Tech, Blacksburg, VA, USA
[2]US Naval Research Laboratory, Washington DC, USA

Abstract

The generation of plasma from hypervelocity impacts is an active research topic due to its important science and engineering ramifications in various applications. Previous studies have mainly focused on the ionization of the solid materials that constitute the projectile and the target. In this letter, we consider impact events that occur in a fluid (e.g., gas) medium, and present a multiphysics computational modeling approach and associated analysis to predict the behavior of the dynamic fluid-solid interaction that causes the surrounding fluid to ionize. The proposed computational framework is applied to a specific case involving a system of three interacting domains: a copper rod projectile impacting onto a soda lime glass target in a neon gas environment. The impact velocity is varied between 3 km/s and 6 km/s in different simulations. The computational model couples the compressible inviscid Navier-Stokes equations with the Saha ionization equations. The three material interfaces formed among the projectile, the target, and the ambient gas are tracked implicitly by solving two level set equations that share the same velocity field. The mass, momentum, and energy fluxes across the interfaces are computed using the FInite Volume method with Exact two-material Riemann problems (FIVER). The simulation result reveals a region of neon gas with high velocity, temperature, pressure, and mass density, formed in the early stage of the impact mainly due to the hypersonic compression of the fluid between the projectile and the target. For impact velocities higher than 4 km/s, ionization is predicted in this region.

1 Introduction

Hypervelocity impact describes the collision of a solid projectile onto a target structure at a velocity that exceeds the speed of sound in the target medium. It features the rapid transport and dissipation of kinetic energy through mechanical, thermal, chemical, and electromagnetic pathways; and is relevant to many applications in geological and planetary sciences, aerospace engineering, and defense engineering [1–4]. In the past, extensive research has been conducted to understand and predict the mechanical response and failure of the target and the projectile, including shock waves, deformation, fracture, and fragmentation [5–9]. It has also been found that the temperature behind an impact-induced shock wave may exceed thousands of Kelvin, causing the material to ionize, thereby producing a complex plasma mixture (Fig. 1(a)) [2, 10]. Scientific studies on impact-generated plasma can be traced back to Friichtenicht and Slattery (1963) [11], if not earlier. Since then, various authors have published data that characterize the composition and energy of plasma generated under different impact conditions (e.g., [12–14]). Electromagnetic waves emitted by impact-generated plasma have also been detected in laboratory experiments. For example, Bianchi *et al.* [15] captured electromagnetic pulses in the radio frequency range from experiments with shaped charges accelerated to 10 km/s.

In the last decade, there has been a growing interest in developing models and numerical tools to predict and characterize impact-generated plasma and electromagnetic waves. This trend has been largely aligned with the rising concern of collisions between space vehicles and space debris. In this context, the electromagnetic waves emitted by an impact-generated plasma may pose a threat to the function and safety of on-board electronic devices [16]. For example, Li *et al.* simulated hypervelocity impact of aluminum projectiles and targets for impact velocities between 5 and 10 km/s [17, 18]. They developed a smoothed particle

*Corresponding author. E-mail address: kevinwgy@vt.edu.

hydrodynamics (SPH) solver to simulate the solid dynamics, and used the Thomas-Fermi model to predict temperature and ionization. Fletcher *et al.* [14, 19] also developed an SPH code to simulate hypervelocity impacts, and used the non-ideal Saha equations to predict ionization of the target material. They tested a wider range of impact velocities, between 10 and 72 km/s. Fletcher *et al.* also developed a particle-in-cell code to investigate the mechanism of electromagnetic emission from the impact-generated plasma [20]. Despite these progresses, the generation of plasma and electromagnetic waves from hypervelocity impacts remains an active research area. The determination and explanation of the causal source (i.e. projectile, target, or the surrounding gas) and composition of plasma, the dependence of plasma energy on impact velocity (cf. [12, 13]), and the energy and spectrum of the electromagnetic emissions [20] remain open questions in general.

Previous studies on hypervelocity impact have mainly focused on the dynamic response and material behaviors of the projectile and the target, while the ambient environment is usually assumed to be a vacuum [13, 21–23]. This assumption can be valid when studying collisions that occur in the exoatmospheric space environment. However, for terrestrial and atmospheric applications in which the collision occurs in a fluid medium, the projectile produces a hypersonic fluid flow during its flight, which can easily exceed Mach 10. The collision between the projectile and the target causes a sudden change in the velocity and thermodynamic state on the fluid domain boundary, which leads to the emission of shock waves that propagate through the fluid domain. These impact-induced shock waves disrupt the initial flow field. Depending on the impact velocity and the properties of the fluid material, the energy carried by the shock waves may cause the fluid to ionize, thereby forming a plasma. The atomic and molecular structures of the ambient fluid play an important role on the mechanisms of ionization. The primary ionization mechanism is by collision where a free electron collides with a neutral molecular and gives rise to a new electron and a positive ion, or when negatively charged ions are produced when a free electron collides with an atom and is subsequently trapped inside the electric potential barrier, releasing any excess energy. The secondary ionization mechanisms that may be also involved are the electron emission due to positive ion impact, and the electron emission due to metastable and neutral atoms. All these mechanisms depend on the ionization energy which in turn is related to the atomic number of the gas elements participating in the ambient fluid. Overall, understanding the fluid dynamics, thermodynamics, ionization, and plasma characteristics is important for developing a complete description of hypervelocity impact events that occur in a fluid medium. The knowledge obtained may also lead to the development of new diagnostic tools for hypervelocity impact detection and characterization.

In this letter, we present a computational framework for analyzing the interaction between the projectile, the target, and the ambient fluid during a hypervelocity impact, focusing on the formation of plasma in the fluid. The impact velocity of the projectile is varied between 3 km/s and 6 km/s in different tests. In each test case, the simulation is performed in two steps, including a steady-state computational fluid dynamics (CFD) analysis that generates the initial fluid flow around the projectile, followed by a fluid-solid coupled analysis of the impact process. In Section 2, we present the geometry, model equations, and numerical methods involved in this study. In Section 3, we present and discuss the obtained numerical results, including the time histories of pressure, velocity, temperature, and average charge number. Finally, some concluding remarks are provided in Section 4.

2 Physical model and computational methods

As a model problem, we consider the collision of an oxygen-free high conductivity (OFHC) copper rod projectile onto a soda lime glass target (SLG) in a neon gas environment. Copper projectiles and SLG targets are frequently used in laboratory experiments (e.g. [24, 25]), and thus have been chosen as the respective materials for this computational study. The choice of SLG as the material of the target is further motivated by its potential use in armor and protective systems [26–28]. It is inexpensive, transparent, and has relatively high mechanical strength. Neon gas is selected as the ambient fluid because it is monoatomic, chemically inert, and has a density similar to that of air.

The computational model adopted in this study combines the compressible inviscid Navier-Stokes equations with the Saha ionization equations. We solve the Navier-Stokes equations in the Eulerian reference frame using a high-resolution finite volume method. The spatial domain includes three subdomains, occupied by the projectile, the target, and the surrounding fluid, respectively. The boundaries of the projectile and

the target are represented implicitly as the 0 level set of two signed distance functions [29, 30]. The motion and deformation of these boundaries are predicted by solving two level set equations that share the same velocity field. This method allows us to keep track of three sharp, interconnected material interfaces (i.e. projectile-fluid, target-fluid, and projectile-target) that undergo large, complex deformations. Across the interfaces between neon gas and the solid materials, the density jump can exceed a factor of 10,000, and the thermodynamic relations (i.e. equations of state) also differ significantly. This type of discontinuities pose a challenge to the computation of fluxes across material interfaces. In this work, the mass, momentum, and energy fluxes across material interfaces are computed using the FInite Volume method based on Exact two-material Riemann problem (FIVER) [31–35]. By constructing and solving an exact Riemann problem along each edge in the mesh that crosses a material interface, FIVER explicitly accounts for the change of equation of state across the interface. Previously, it has been validated for several shock-dominated multiphase flow and fluid-structure interaction problems in underwater explosion and implosion, pipeline explosion, cavitation erosion, and shock wave lithotripsy [33, 36–41]. Within the fluid subdomain, we solve the Saha equations coupled with the condition of electroneutrality and mass conservation of nuclei to predict the onset of ionization and the distribution of ionization products. This model assumes local thermodynamic equilibrium, which can be justified for predicting the formation and initial expansion of plasma during hypervelocity impacts [14, 42].

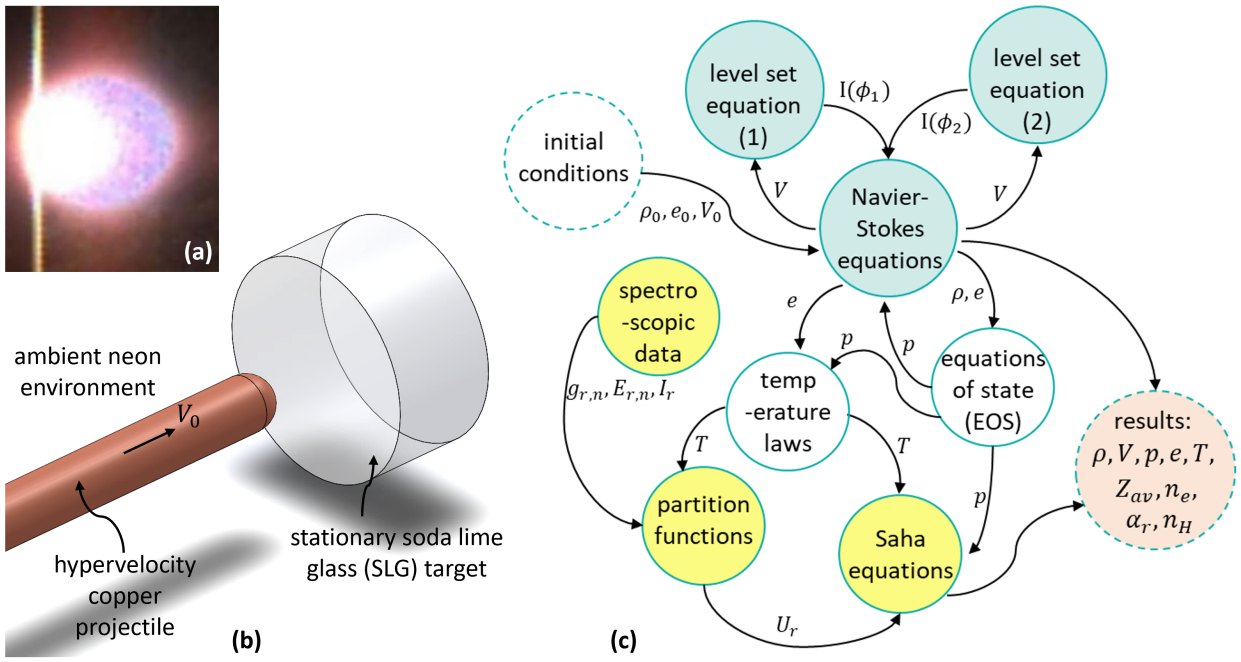

Figure 1: Hypervelocity impact: Problem setup. (a) Hypervelocity impact flash captured in a laboratory experiment [2]. (b) The model problem investigated: A long copper rod impacting on a soda lime glass target in neon gas. The impact velocity, V_0, is varied between 3 km/s and 6 km/s. (c) An overview of the computational multiphysics model used in this study, which accounts for the dynamic interaction between the solid and fluid (gas) materials and fluid ionization.

Figure 1(b) presents the setup of the hypervelocity impact problem investigated in this paper. The projectile is a cylindrical copper rod of 5 mm radius, with a semi-spherical leading edge. The target is an SLG cylinder with a radius of 30 mm and a height of 20 mm. The ambient gas is assumed to be neon, which is inert even at high pressures and temperatures. In the far-field, the gas density, pressure, and temperature are fixed at 0.82 kg/m^3, 100 kPa, and 300 K, respectively. The velocity of the projectile, V_0, is varied between 3 km/s and 6 km/s in different simulations. To put this into context, the bulk speed of sound in SLG and copper are around 4 km/s and 3.7 km/s at room temperature and atmospheric pressure. The speed of sound in neon is 0.46 km/s.

Because of the high impact velocities, the solid materials involved in this problem, namely copper and

SLG, are modeled as compressible fluids. When the impact velocity exceeds 3 km/s, the density of the energy transferred from the projectile to the SLG target is far greater than the strain energy density of SLG. In the past, Kobayashi *et al.* showed that when impacted by steel and tungsten projectiles traveling at 4 km/s to 6 km/s, the maximum pressure inside SLG exceeds 50 GPa [10], which is one order of magnitude higher than the material's Hugoniot elastic limit (3 GPa to 8 GPa) [25, 43–47].

Therefore, the dynamics of the target, the projectile, and the surrounding gas can be considered to be governed by the three-dimensional (3D) compressible Navier-Stokes equations. In addition, we neglect the effects of viscosity and heat diffusion, which reduces the Navier-Stokes equations to

$$\frac{\partial}{\partial t}\begin{bmatrix}\rho\\ \rho V\\ \rho e_t\end{bmatrix} + \nabla\cdot\begin{bmatrix}\rho V^T\\ \rho V\bigotimes V + p\mathbf{I}\\ (\rho e_t + p)V^T\end{bmatrix} = 0, \tag{1}$$

also known as the Euler equations. Here ρ, V, e_t, p denote density, velocity, total energy per unit mass, and pressure, respectively. $\mathbf{I}$ is the three-dimensional (3D) identity matrix.

At any time $t \geq 0$, the physical domain Ω consists of three material subdomains, occupied by neon, copper, and SLG, respectively. Across material interfaces, pressure and the normal component of velocity are continuous, whereas density and the tangential components of velocity are generally discontinuous. Equation (1) is algebraically closed by a thermodynamic equation of state (EOS) for each material. The monoatomic configuration and the absence of valence electrons entail that neon atoms have only translational degrees of freedom, but not vibrational, rotational, or electronic degrees of freedom. Therefore, the specific heat of neon is independent of temperature [48], which justifies the use of the calorically perfect gas EOS. The copper projectile is modeled using the Mie-Grüneisen EOS [49], i.e.

$$p(\rho, e) = \frac{\rho_0 c_0^2 \eta}{(1-s\eta)^2}\left(1 - \frac{1}{2}\Gamma_0\eta\right) + \rho_0\Gamma_0 e, \tag{2}$$

where ρ_0 and c_0 denote the density and bulk speed of sound in the ambient condition. s is the slope of the Hugoniot curve. Γ_0 is the Grüneisen parameter. $\eta = 1 - \rho_0/\rho$. The SLG target is modeled using the stiffened gas EOS [50], i.e.

$$p(\rho, e) = (\gamma - 1)\rho e - \gamma p_c, \tag{3}$$

where γ and p_c are empirical model parameters. The SLG material is not modeled using the Mie-Grüneisen EOS, because certain regions in the SLG target experience high tensile stresses during hypervelocity impact, while the Mie-Grüneisen EOS has been primarily used to model materials in compression [49]. On the other hand, the stiffened gas EOS can be calibrated to capture the shock Hugoniot obtained from laboratory experiments [50]. Specifically, we combine Eq. (3) with the Rankine-Hugoniot jump conditions, then fit them to the shock Hugoniot, $u_s = c_0 + su_p$, obtained from laboratory impact experiments, where u_s and u_p denote the shock speed and the downstream particle velocity, respectively. The shock Hugoniot data presented in [45] ($c_0 = 2.01$ km/s, $s = 1.7$) is adopted in this work, which gives $\gamma = 3.9$ and $p_c = 2.62$ GPa. All the EOS parameters used in the simulations are presented in Table 1.

Substance	EOS	Parameters			
Copper	Mie-Grüneisen	c_0 (km/s)	s	ρ_0 (kg/m^3)	Γ_0
		3.93 [51]	1.50 [51]	8960	2.12 [52]
Soda lime glass (SLG)	Stiffened gas	γ	p_c (GPa)		
		3.9	2.62		
Neon	Perfect gas	γ	c_p (J/(K · kg))		
		1.667	618.3		

Table 1: Parameters of the equations of state for copper, SLG, and neon.

Each simulation is performed in two steps. First, a steady-state computational fluid dynamics (CFD) analysis is performed to capture the hypersonic fluid flow surrounding the projectile in flight, which features a

curved bow shock (Fig. 2(a)). Next, a fluid-solid coupled impact analysis is performed to predict the dynamic interaction between the projectile, the target, and the surrounding gas, including the possible ionization of the gas. The impact analysis is initialized at a time shortly before the bow shock reaches the target, and the steady-state CFD result is used as the initial condition within the fluid subdomain (Fig. 2(b)). In both steps, the Navier-Stokes equations (Eq. (1)) are solved using a finite volume method. The steady-state CFD analysis is performed using the AERO-F solver [53] on an unstructured, body-fitted mesh. In the most refined region, the characteristic element size is approximately 0.15 mm. The fluid-solid coupled impact analysis is performed using the M2C solver [54] on a non-body-fitted Cartesian mesh. In the most refined region, the element size is 0.1 mm.

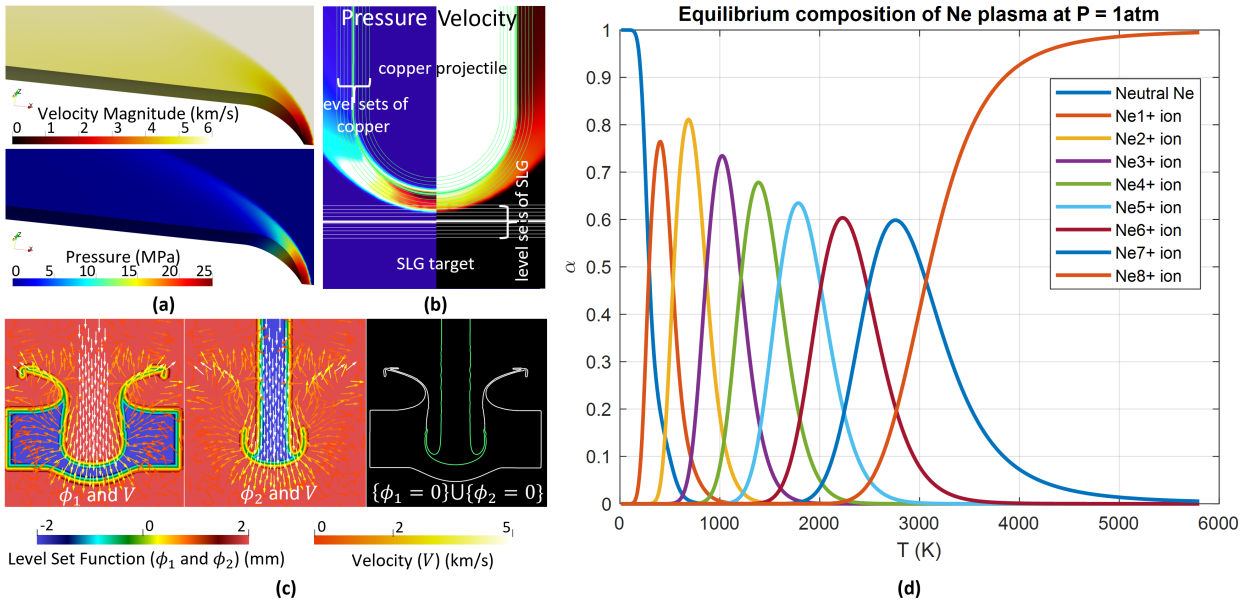

Figure 2: Major components of the computational framework. (a) Simulation of the hypersonic fluid flow surrounding the projectile before the collision through a steady-state, body-fitted CFD analysis. (b) Initialization of the fluid-solid coupled impact analysis. The fluid density, velocity, and pressure fields obtained from the CFD analysis are mapped to a new mesh that does not resolve the boundaries of the projectile and the target. (c) Implicit tracking of the three material interfaces between the projectile, the target, and the ambient gas by solving two level set equations that share the same velocity field. (d) Solution of the Saha equations for neon (Ne) at the atmospheric pressure and different temperatures between 0 and 6000 K. The plotted result (α) is the molar fractions of neon atoms and ions with different charge numbers (0 - 8 shown here).

In the impact analysis, the material interfaces are tracked implicitly using the level set method [29, 30]. Specifically, two level set equations of the form

$$\frac{\partial \phi_s}{\partial t} + V \cdot \nabla \phi_s = 0, \qquad s = 1, 2 \tag{4}$$

are solved synchronously to track the boundaries of the copper projectile and the SLG target, respectively. The two level set functions, ϕ_1 and ϕ_2, are initialized to be the signed distance from each point in the computational domain to the surface of the target and the projectile, respectively. Notably, the two level set equations share the same velocity field. As a result, the contact and separation between the projectile and the target are captured naturally, while spurious overlaps are avoided (Fig. 2(c)). The mass, momentum, and energy fluxes across material interfaces are computed using the method of FIVER (FInite Volume method based on Exact multiphase Riemann solvers), which has been validated for several multiphase flow problems featuring large density jumps [33, 39, 41]. Following this method, a one-dimensional bimaterial Riemann problem is constructed along each edge in the mesh that crosses a material interface. The solution of this exact Riemann problem is used to compute the local fluxes.

In the impact analysis, the onset and extent of ionization in the ambient neon gas, under the assumption of non-interacting electrons and ions, is predicted by the Saha equations, i.e.

$$\frac{n_{r+1}n_e}{n_r} = 2\frac{U_{r+1}}{U_r}\left[\frac{2\pi m_e k_B T}{h^2}\right]^{3/2}\exp\left(\frac{-I_r}{k_B T}\right), \qquad r = 0, 1, ..., N, \tag{5}$$

where n_r is the number density of the r-th charge state ion, n_e is the number density of electrons (also referred to as the plasma density), T is the temperature, h is the Planck constant, k_B is the Boltzmann constant, m_e is the stationary mass of an electron, and I_r the r-th ionization energy. For neon, N is equal to 9.

In this work, we couple the Saha equations with the condition of quasi-neutrality (i.e. conservation of charge) and the conservation of nuclei, which yields the one dimensional transcendental equation [55],

$$Z_{\text{av}}\Big(1 + \sum_{r=1}^{N}\frac{\prod_{m=1}^{r} f_m}{(Z_{\text{av}}n_H)^r}\Big) = \sum_{r=1}^{N}\Big(\frac{r}{(Z_{\text{av}}n_H)^r}\prod_{m=1}^{r} f_m\Big), \tag{6}$$

where Z_{av} denotes the average charge number of neon, and n_H the number density of heavy particles. f_m is given by

$$f_m = 2\frac{U_{m+1}}{U_m}\Big(\frac{2\pi m_e k_B T}{h^2}\Big)^{\frac{3}{2}}\exp\Big(-\frac{I_m}{k_B T}\Big). \tag{7}$$

U_r is the state-dependent partition function of the r-th charge state ion, given by

$$U_r = \sum_{n=1}^{\infty} g_{r,n}\exp\left(-\frac{E_{r,n}}{k_B T}\right), \tag{8}$$

where $g_{r,n}$ and $E_{r,n}$ denote the degeneracy and excitation energy of the r-th ion at the n-th energy level. In this work, the values of I_r, $E_{r,n}$, and $g_{r,n}$ for neon are obtained from the NIST atomic spectra database [56]. Sample spectroscopic data are shown in Table 2 for the atomic neon and the first three ionic stages (i.e. $r = 0, 1, 2, 3$). The ionization energy for each state, along with the excitation energies and their corresponding degeneracies for the first three electronic energy levels (i.e. $n = 1, 2, 3$) are shown in the table. In the simulations, up to 1943 levels are accounted for in the solution of the Saha equations.

r	I_r(eV)	n	$g_{r,n}$	$E_{r,n}$(eV)
0	21.565	1	1	0.000
		2	5	16.619
		3	3	16.671
1	40.963	1	4	0.000
		2	2	0.967
		3	2	26.910
2	63.423	1	5	0.000
		2	3	0.080
		3	1	0.114
3	97.190	1	4	0.000
		2	6	5.112
		3	4	5.118

Table 2: Sample spectroscopic data of neon for $r = 0, 1, 2, 3$ and $n = 1, 2, 3$ [56]. I_r denotes the ionization energy of the r-th charge state ion. $g_{r,n}$ denotes the degeneracy of an electron of the r-th ion at the n-th energy level, and $E_{r,n}$ its corresponding excitation energy.

In each time step, we solve Eq. (6) for Z_{av} using a safeguarded iterative method, TOMS748 [57], at each node within the subdomain occupied by neon. After that, the plasma density and molar fraction of each ion

state can be easily calculated following the method described by Zaghloul *et al.* [55]. The molar fraction, α, of the r-th ion is the ratio of the number density of said ion to the total number density of heavy particles. To accelerate the solution process, we tabulate $U_r,\ r = 0, 1, \cdots, 10$ as functions of $\exp(-1/T)$ at the beginning of the impact analysis. In each time step, we calculate the values of U_r using cubic spline interpolation. We have verified our Saha equation solver against the results presented by Zaghloul *et al.* [58]. As an example, Figure 2(d) presents the variation of molar fractions of neon ions at a fixed pressure, $p_0 = 101$ kPa, for temperatures between 0 and 6000 K.

In summary, Fig. 1(c) presents the schematic of the computational framework adopted in this study. The two solvers used in this study, namely AERO-F [53] and M2C [54], are both publicly available.

3 Results and discussion

Figure 3 shows (from left to right) the pressure, velocity magnitude, temperature, and average charge number of neon predicted by the M2C solver for a representative test case with impact velocity $V_0 = 5$ km/s. The figure displays the fields at progressive time instances of (from top to bottom) 0.625 μs, 1.25 μs, 2.5 μs, 5 μs. The collision between the projectile and the target occurs at 0.4 μs.

The emission of shock waves can be observed from the snapshots taken at $t = 0.625$ μs. These include a forward-propagating shock wave in the target, a backward-propagating shock wave in the projectile, and a shock wave in the fluid that expands from the point of collision. The high rate of energy transfer manifests itself in the strong compression waves. In both the projectile and the target, the pressure behind the shock wave reaches 80 GPa at this time. This pressure is one order of magnitude higher than the Hugoniot elastic limit of SLG, and is of similar magnitude to experimental values reported by Kobayashi *et al.* [10]. This observation justifies modeling SLG as a fluid, since the elasticity of the material can be neglected in this pressure regime. In the neon fluid, the peak pressure behind the shock front is around 300 MPa. This is one order of magnitude higher than the peak pressure of the bow shock (cf. Fig. 2(a)), but two orders of magnitude lower than the peak pressure in the solid materials. As such, the pressure plots in Fig. 3 have been scaled to show mainly the variations within the projectile and the target.

At $t = 0.625$ μs, high temperatures can be observed in the fluid subdomain behind the shock wave. This leads to the formation of highly ionized pockets of neon plasma, which expands radially outwards from the point of collision. The mechanism of this plasma formation is investigated in Fig. 4. Specifically, Fig. 4(a) presents a local view of the pressure, velocity, temperature, and average charge number, rescaled to better visualize their variations in a plasma pocket. The neon fluid in the pocket expands outwards at a typical velocity of 10 km/s, which is twice the impact velocity. Similar ratios are observed for other tested impact velocities between 3 and 6 km/s. Figure 4(a) also shows that the average charge number (Z_{av}) is the highest near the point of impact, and then drops off radially. Nonetheless, the plasma density, n_e, given by

$$n_e = Z_{\text{av}} n_H = Z_{\text{av}} \rho N_A / M, \tag{9}$$

is fairly constant within the pocket, in the order of 10^{17} m^{-3}. Here, N_A is the Avogadro constant, and M the molar mass of neon. This behavior can be explained by the fact that the mass density of neon (ρ) increases within the pocket in the radial directions. The high velocities in this region can be explained by a rudimentary analysis, shown in Fig. 4(b). Consider a fluid particle near the point of collision. Right before collision occurs, this particle moves at a velocity similar to the impact velocity of the projectile. A short time, Δt, after collision, the particle will have traveled roughly a distance of $V_0 \Delta t / \tan(\theta)$, where θ is the instantaneous tangential angle between the projectile and the target. This corresponds to a particle velocity of approximately $V_0 / \tan(\theta)$. For the blunt projectile used in this study, θ is 0 at the initial time of collision, and remains very small shortly thereafter. Therefore, the velocity of the fluid particle can be far greater than the impact velocity, as observed in Fig. 4(b). The impact also rapidly compresses the fluid in this region, resulting in high pressures, which in turn leads to high temperatures and ionization.

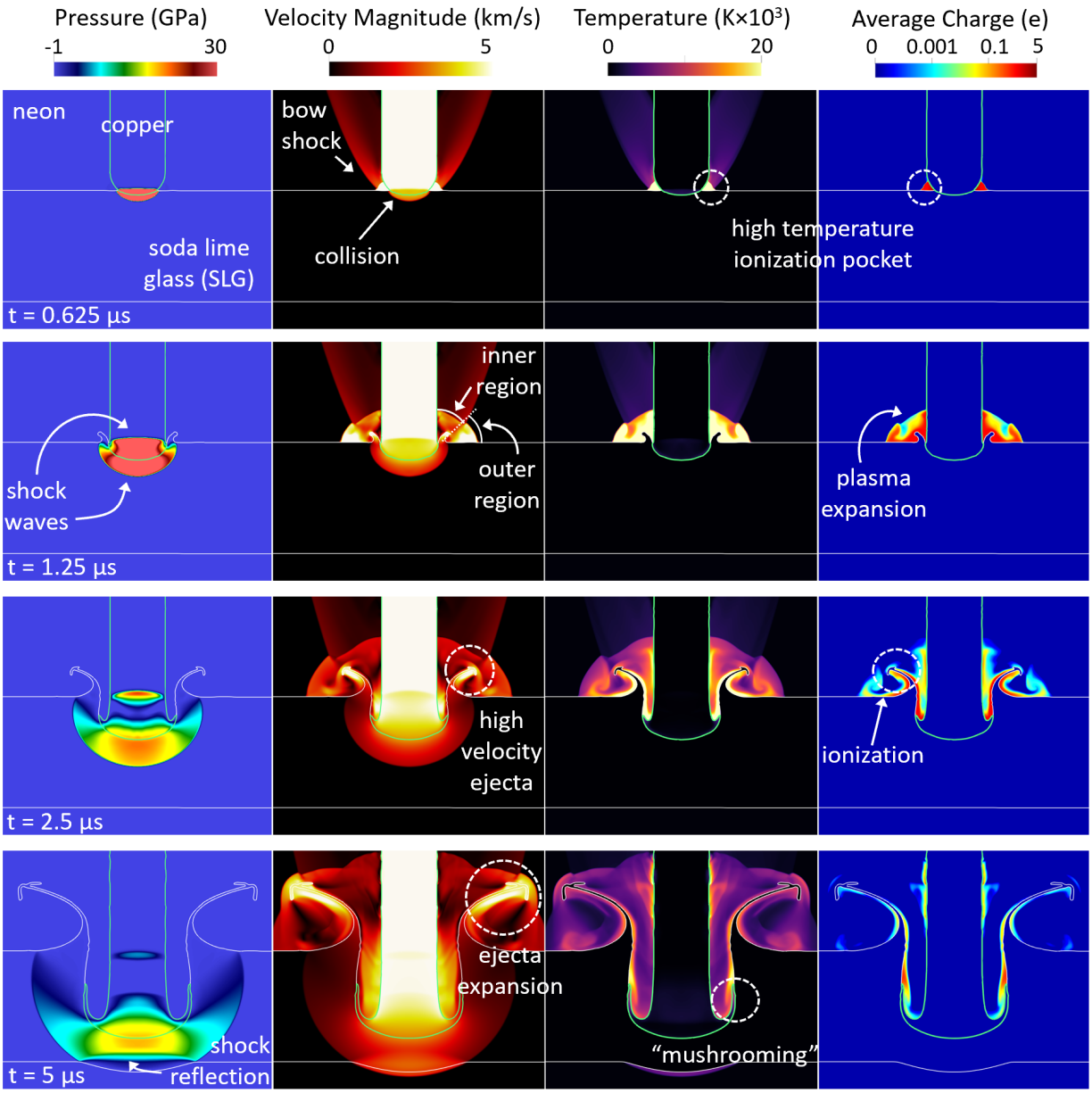

Figure 3: Time evolution of state variables for a hypervelocity impact of copper projectile hitting an SLG target at 5 km/s. From left to right, the pressure, velocity magnitude, temperature, and average charge fields are shown at times of 0.625 μs, 1.25 μs, 2.5 μs, and 2.5 μs (top to bottom). The temperature and average charge fields are computed only in the subdomain occupied by neon, as the present study focuses on the ionization of the ambient fluid.

It is noteworthy that the bow shock generated during the flight of the projectile reaches the target before collision occurs. Remnants of this bow shock can still be observed from the velocity and temperature fields at $t = 0.625$ μs, 1.25 μs, and 2.5 μs (Fig. 3). However, a comparison of the state variables behind the bow shock and within the plasma pockets shows that the effect of the bow shock is negligible relative to that of the collision. To this end, typical values of fluid velocity, pressure, and average charge number are shown in Table 3. In particular, the bow shock does not cause notable ionization in the neon gas, while the average charge number of neon within the impact-generated plasma pocket is around +1.

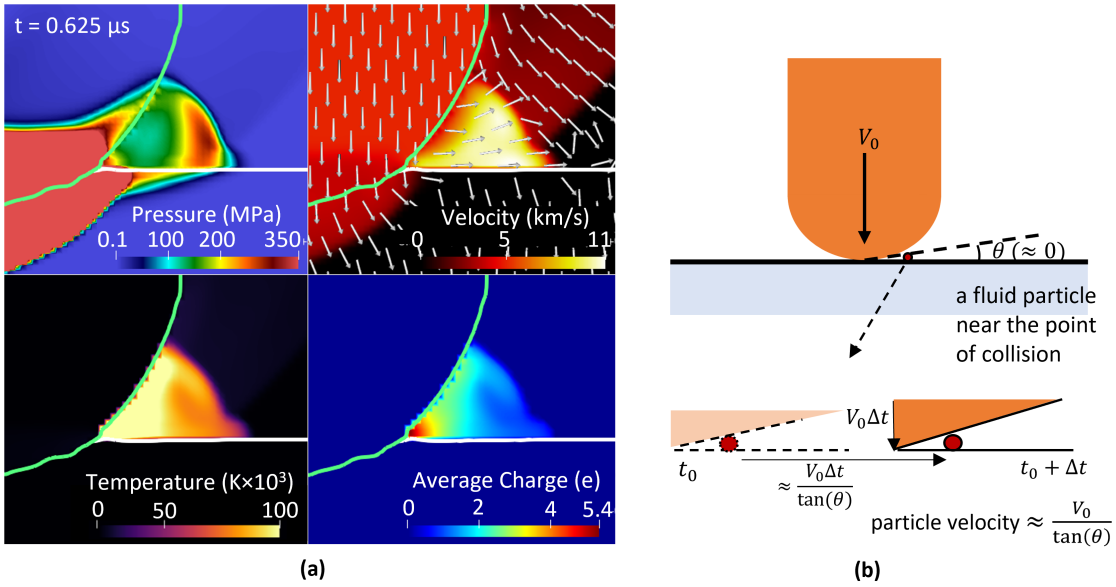

Figure 4: Formation of a neon plasma pocket shortly after collision. (a) State variable fields at $t = 0.625$ μs, showing a pocket of neon compressed by the hypervelocity projectile ($V_0 = 5.0$ km/s) and the target, resulting in high velocity, high temperature, and the formation of a dense plasma. (b) A rudimentary analysis explaining the high fluid velocity in the pocket.

	Behind the bow shock	In the plasma pocket
Velocity magnitude $\|V\|$ (km/s)	2.5	10
Pressure p (MPa)	7.5	300
Average charge number Z_{av} (e)	1×10^{-8}	1

Table 3: Typical values of state variables behind the bow shock and in the plasma pocket, at $t = 0.625$ μs.

The impact causes the formation of a crater in the target. This process is captured in Fig. 3 by the snapshots taken at $t = 1.25$ μs, 2.5 μs, and 5.0 μs. During this process, the SLG material from the rim of the crater is ejected into the neon gas in an explosive manner. The tip of the ejecta moves at roughly the impact velocity throughout the simulation, which causes the body of the ejecta to experience high tensile stress. The ejecta divides the fluid subdomain into an inner region and an outer region, as marked in Fig. 3. The outer region contains the plasma pocket that had initially formed due to the rapid compression of the neon gas between the projectile and the target. At $t = 1.25$ μs, it can be seen that the plasma pockets are expanding rapidly due to the expanding ejecta. This results in a difference between the velocity of neon in the outer region (∼7 km/s) and that in the inner region (∼1 km/s). The inner region evolves into the crater in the target. Rapid deceleration occurs in the region of the projectile that comes in contact with the initially static target, while the main body of the projectile still moves at the impact velocity. This causes the leading edge of the projectile to morph into a "mushroom head" structure, as seen in the snapshots taken at $t = 5$ μs (Fig. 3). This type of mushrooming deformation has been observed in previous studies [59].

It is evident that the rapid expansion and deformation of the SLG ejecta also causes the surrounding neon gas to ionize. This region of ionization is marked in the average charge plot in Fig. 3 at $t = 2.5$ μs. Within this region, neon has high temperature, but low mass density ($\sim 10^{-2}$ kg/m^3). The plasma density within this region is significantly lower than what was found earlier in the plasma pockets.

Inside the SLG target, the energy density behind the shock front decreases as the shock wave expands. When the shock front reaches the back wall of the target, it causes the wall to deform in the radial directions. At the same time, the compressive shock wave is reflected as a tensile wave, which interferes with the incident shock wave. This behavior is captured in Fig. 3, in the snapshots taken at $t = 5$ μs.

In summary, the results obtained from the 5 km/s impact test (Figs. 3 and 4) show that the collision between the projectile and the target causes the surrounding neon gas to ionize, thereby forming a plasma. The primary mechanism of plasma formation is found to be the rapid compression of the neon gas between the projectile and the target.

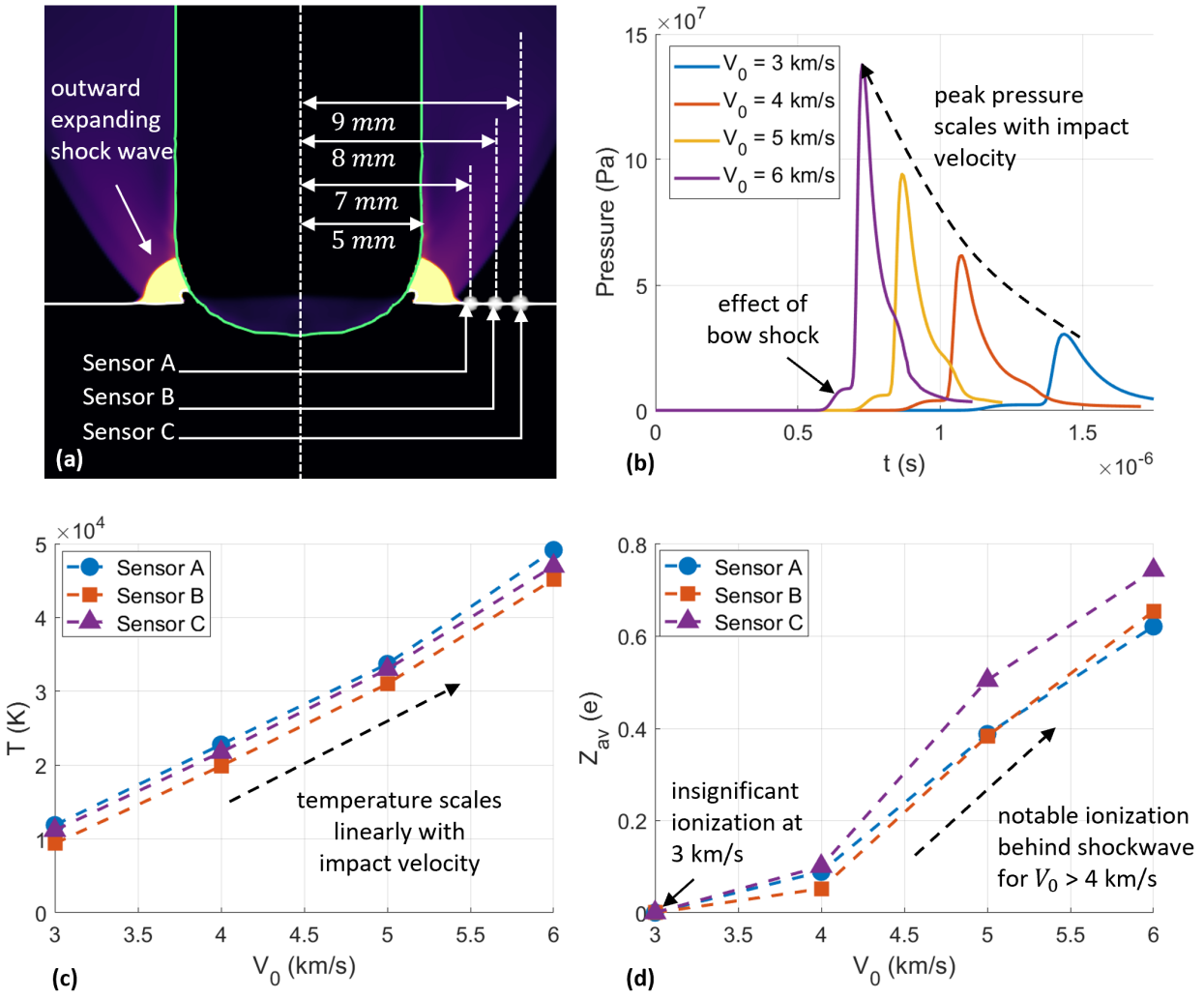

Figure 5: Effects of the impact velocity (V_0) on the thermodynamics and ionization of neon. (a) Location of three virtual sensors (A, B, and C) in neon. (b) Time history of pressure at Sensor A. (c) Peak temperature at each sensor (d) Peak average charge at each sensor

To investigate the effects of impact velocity (V_0) on the dynamics, thermodynamics and ionization of neon, additional impact tests are performed for V_0 between 3 and 6 km/s. In each test, three virtual sensors are positioned 1 mm above the SLG target and at radial distance r = 7, 8, and 9 mm, respectively. The sensors are labeled as A, B, and C, as shown in Fig. 5 (a). The time-histories of pressure, temperature, and average charge number are recorded at the sensor locations. Specifically, Fig. 5(b) shows the pressure time-histories at Sensor A for V_0 = 3, 4, 5, and 6 km/s. In each case, a sharp pressure pulse is captured, corresponding to the arrival of the shock wave propagating in the neon gas. As V_0 increases, the peak pressure increases monotonically from approximately 30 MPa to 140 MPa. As time progresses, the pressure at the sensor location drops off rapidly. Eventually, the ejecta collides with the sensor, and the reading is terminated at that time instance. Finally, Fig. 5(c) and (d) show the maximum values of temperature (T) and average charge number (Z_{av}) of neon at the three sensor locations. As impact velocity increases from 3 to 6 km/s, the maximum temperature increases almost linearly at all the sensors locations. The average

charge number also increases with impact velocity, but in a nonlinear fashion. At 3 km/s, the maximum value of Z_{av} is found to be less than 10^{-3} at all the sensor locations, which indicates that ionization is insignificant. As impact velocity exceeds 4 km/s, Z_{av} quickly increases, showing noticeable ionization. At 6 km/s, the maximum value of Z_{av} reaches 0.74 at Sensor C. In this case, the plasma density is of the order of 10^{17} m^{-3} at all the sensor locations.

In an earlier computational analysis, Fletcher *et al.* [14] showed that Z_{av} in the solid materials becomes significant at impact velocities greater than 18 km/s. In comparison, our result suggests that the ambient fluid may ionize at much lower impact velocities. This can be explained by the higher temperatures behind the shock waves in the ambient fluid than in the solids. For example, the temperatures in the neon gas (see Fig. 5(c)) is one order of magnitude greater than the experimental data recorded by Kobayashi *et al.* [10] in SLG at similar impact velocities. As such, the plasma formed in the ambient fluid from atmospheric hypervelocity impacts may play an important role in the overall dynamics and characteristics of the impact generated plasma.

4 Conclusions

This letter presents a computational analysis of hypervelocity impact events that occur in a fluid medium. The analysis focuses on predicting the formation of plasma in the surrounding fluid, and finding the possible mechanisms that may cause the fluid to ionize. The projectile, target, and ambient fluid materials used in this study are copper, soda lime glass (SLG), and neon, respectively. The projectile is in the shape of a cylindrical rod, with a semi-spherical leading edge. The impact velocity is varied between 3 km/s and 6 km/s in different tests. The computational framework developed for this study couples a compressible Navier-Stokes equations solver with a Saha ionization equations solver. Compared to conventional impact simulators, a notable difference of the current framework is that the computational domain includes the ambient fluid as a material subdomain, and the fluid's dynamics, thermodynamics, and ionization are included in the physical model. Also, the shock-dominated hypersonic flow around the flying projectile is captured through a steady-state computational fluid dynamics (CFD) analysis, and prescribed as an initial condition for the impact analysis.

The inclusion of the ambient fluid leads to two computational challenges. First, the domain includes three internal material interfaces between the projectile, the target, and the ambient fluid. These interfaces are interconnected (in the sense that triple points exist), and undergo large, complex deformation during the impact. In this study, the interfaces are tracked implicitly by solving two level set equations that share the same velocity field. This method maintains sharp (i.e. 0 thickness) interfaces, and naturally avoids spurious overlapping and separation between different material subdomains. Second, the state variables and thermodynamic relations change drastically across the solid-gas interfaces. To account for this type of discontinuities, the recently developed FIVER method is employed. When computing numerical fluxes across a material interface, FIVER constructs and solves an exact bimaterial Riemann problem using the correct equations of state on both sides of the interface.

The main finding of this study is that for impact velocities greater than 4 km/s, ionization of neon is predicted in the early stage of the impact, adjacent to the point of collision. The ionized region is behind the shock front in the ambient gas, referred to as plasma pockets in the letter. Within this region, neon has high temperature, pressure, velocity, and mass density. Moreover, the plasma density (i.e. electron number density) reaches the order of 10^{17} m^{-3} in the test case with an impact velocity of 6 km/s. The simulation results suggest that the main cause of ionization in this region is the rapid compression of the neon gas between the hypervelocity projectile and the target. The high velocity in the region can also be related to the geometry of the projectile, particularly, the blunt leading edge. As time progresses, the size of the plasma pockets increases, while the intensity decreases. Meanwhile, the SLG material at the rim of the impact crater is ejected into the ambient environment in an explosive manner, which also causes the surrounding neon to ionize. Nonetheless, the effect of this mechanism is insignificant compared to the hypervelocity compression that formed the plasma pockets. The computational analysis also captures the impact of the bow shock in the neon gas on the SLG target, which occurs before the collision. The effect of the bow shock is found to be insignificant compared to that of the collision. Following these findings, additional work is needed to design and perform a validation study, and to investigate the sensitivity of plasma density with respect to

geometric and material properties, possibly over a broader range of impact velocities.

Acknowledgment

S.T.I, W.M., and K.W. gratefully acknowledge the support of the Office of Naval Research (ONR) under Award N00014-19-1-2102. J.G.M. gratefully acknowledges the support of the ONR under award N00014-21-WX01554.

Declaration of interests

The authors declare that they have no known competing financial interests or personal relationships that could have appeared to influence the work reported in this paper.

References

1. Jiang, H., Scott, V. & Li, B. Modeling and simulations of high and hypervelocity impact of small ice particles. *International Journal of Impact Engineering* **155,** 103906 (2021).
2. Barsoum, R. G. *Shockwave compression physics of condensed matter lattice Boltzmann method with application to glass under hypervelocity impact* (2019).
3. Asimow, P. D. *et al.* Shock synthesis of quasicrystals with implications for their origin in asteroid collisions. *Proceedings of the National Academy of Sciences* **113,** 7077–7081 (2016).
4. Lawrence, R., Reinhart, W., Chhabildas, L. & Thornhill, T. Spectral measurements of Hypervelocity Impact Flash. *International Journal of Impact Engineering* **33,** 353–363 (2006).
5. Whipple, F. Meteorites and space travel. *Astronomical Journal* **52,** 137 (1947).
6. Schonberg, W. P. Hypervelocity Impact Penetration Phenomena in Aluminum Space Structures. *Journal of Aerospace Engineering* **3,** 173–185. (2022) (July 1990).
7. Cour-Palais, B. G. Hypervelocity impact in metals, glass and composites. *International Journal of Impact Engineering* **5,** 221–237. (2022) (Jan. 1987).
8. Li, B, Kidane, A, Ravichandran, G & Ortiz, M. Verification and validation of the Optimal Transportation Meshfree (OTM) simulation of terminal ballistics. *International Journal of Impact Engineering* **42,** 25–36 (2012).
9. Birnbaum, A. J., Steuben, J. C., Iliopoulos, A. P. & Michopoulos, J. G. Simulating hypervelocity impact and material failure in Glass. *Volume 1B: 38th Computers and Information in Engineering Conference* (2018).
10. Kobayashi, T., Sekine, T., Fat'yanov, O. V., Takazawa, E. & Zhu, Q. Y. Radiation temperatures of soda-lime glass in its shock-compressed liquid state. *Journal of Applied Physics* **83,** 1711–1716 (1998).
11. Friichtenicht, J. F. & Slattery, J. C. *Ionization associated with hypervelocity impact* tech. rep. (1963).
12. Ratcliff, P. R., Burchell, M. J., Cole, M. J., Murphy, T. W. & Alladfadi, F. Experimental measurements of hypervelocity impact plasma yield and Energetics. *International Journal of Impact Engineering* **20,** 663–674 (1997).
13. Lee, N. *et al.* Theory and experiments characterizing hypervelocity impact plasmas on biased spacecraft materials. *Physics of Plasmas* **20,** 032901 (2013).
14. Fletcher, A., Close, S. & Mathias, D. Simulating plasma production from hypervelocity impacts. *Physics of Plasmas* **22,** 093504 (2015).
15. Bianchi, R. *et al.* Radiofrequency emissions observed during macroscopic hypervelocity impact experiments. *Nature* **308,** 830–832 (1984).
16. Lee, N. *Understanding spacecraft electrical anomalies: Theory and experiments characterizing hypervelocity impact plasma dynamics* (Stanford University, 2012).

17. Song, W., Li, J. & Ning, J. Characteristics of plasma generated by hypervelocity impact. *Physics of Plasmas* **20,** 093501 (2013).

18. Li, J., Song, W. & Ning, J. Theoretical and numerical predictions of Hypervelocity Impact-generated plasma. *Physics of Plasmas* **21,** 082112 (2014).

19. Fletcher, A. *Plasma production and radiation from meteoroid impacts on spacecraft* PhD thesis (2015).

20. Fletcher, A. C. & Close, S. Particle-in-cell simulations of an RF emission mechanism associated with Hypervelocity Impact Plasmas. *Physics of Plasmas* **24,** 053102 (2017).

21. McBride, N. & McDonnell, J. A. Meteoroid impacts on spacecraft:: sporadics, streams, and the 1999 Leonids. *Planetary and Space Science* **47,** 1005–1013 (1999).

22. Harano, T. *et al.* Preliminary study on sustained arc due to plasma excited by hypervelocity impact of space debris on the solar array coupon. *International Journal of Impact Engineering* **33,** 326–334 (2006).

23. Zhang, K., Long, R., Zhang, Q., Xue, Y. & Ju, Y. Flash characteristics of plasma induced by hypervelocity impact. *Physics of Plasmas* **23,** 083519 (2016).

24. Joshi, A., Ravindran, S., Gandhi, V. & Ravichandran, G. Probing the properties and mechanisms of failure waves in soda-lime glass. *Journal of Applied Physics* **129,** 185902 (2021).

25. Alexander, C. S. *et al.* The hugoniot elastic limit of soda-lime glass. *AIP Conference Proceedings* (2007).

26. Alexander, C. S. *et al. Status of Glass Experiments at Sandia National Laboratories.* tech. rep. (Sandia National Lab.(SNL-NM), Albuquerque, NM (United States); Sandia ..., 2006).

27. Monroe, K. A. *Time-Resolved Fractoluminescence Characterization in Soda-Lime Glass Via Near Hypervelocity Kinetic Impact Fast Fracture* MA thesis (Monterey, CA; Naval Postgraduate School, 2021).

28. Cachiaras, A., Gilde, L., Swab, J. J., Patel, P. J. & Quinn, G. D. *Soda-lime-silicate float glass: A property comparison* tech. rep. (US Army Research Laboratory Aberdeen Proving Ground United States, 2017).

29. Sethian, J. A. & Sethian, J. A. *Level set methods and fast marching methods: Evolving interfaces in computational geometry, Fluid Mechanics, computer vision, and materials science* (Cambridge University Press, 1999).

30. Osher, S. & Fedkiw, R. P. *Level set methods and dynamic implicit surfaces* (Springer, 2009).

31. Farhat, C., Rallu, A. & Shankaran, S. A higher-order generalized ghost fluid method for the poor for the three-dimensional two-phase flow computation of underwater implosions. *Journal of Computational Physics* **227,** 7674–7700 (2008).

32. Farhat, C., Gerbeau, J.-F. & Rallu, A. Fiver: A finite volume method based on exact two-phase Riemann problems and sparse grids for multi-material flows with large density jumps. *Journal of Computational Physics* **231,** 6360–6379 (2012).

33. Wang, K. G., Lea, P. & Farhat, C. A computational framework for the simulation of high-speed multi-material fluid-structure interaction problems with dynamic fracture. *International Journal for Numerical Methods in Engineering* **104,** 585–623 (2015).

34. Main, A., Zeng, X., Avery, P. & Farhat, C. An enhanced fiver method for multi-material flow problems with second-order Convergence Rate. *Journal of Computational Physics* **329,** 141–172 (2017).

35. Ho, J. & Farhat, C. Discrete embedded boundary method with smooth dependence on the evolution of a fluid-structure interface. *International Journal for Numerical Methods in Engineering* **122,** 5353–5383 (2021).

36. Farhat, C. *et al.* Dynamic implosion of underwater cylindrical shells: Experiments and computations. *International Journal of Solids and Structures* **50,** 2943–2961 (2013).

37. Wang, K. G. Multiphase fluid-solid coupled analysis of shock-bubble-Stone Interaction in Shockwave Lithotripsy. *International Journal for Numerical Methods in Biomedical Engineering* **33** (2017).

38. Cao, S., Zhang, Y., Liao, D., Zhong, P. & Wang, K. G. Shock-induced damage and dynamic fracture in cylindrical bodies submerged in liquid. *International journal of solids and structures* **169,** 55–71 (2019).

39. Cao, S, Wang, G, Coutier-Delgosha, O & Wang, K. Shock-induced bubble collapse near solid materials: Effect of acoustic impedance. *Journal of Fluid Mechanics* **907** (2021).

40. Xiang, G. *et al.* Variations of stress field and stone fracture produced at different lateral locations in a shockwave lithotripter field. *The Journal of the Acoustical Society of America* **150,** 1013–1029 (2021).

41. Ma, W., Zhao, X., Gilbert, C. & Wang, K. Computational analysis of bubble–structure interactions in near-field underwater explosion. *International Journal of Solids and Structures* **242,** 111527 (2022).

42. Chen, F. F. *Introduction to plasma physics and Controlled Fusion* (Springer, 2018).

43. Brar, N. S. & Bless, S. J. Failure waves in glass under dynamic compression. *High Pressure Research* **10,** 773–784 (1992).

44. Rosenberg, Z., Yaziv, D. & Bless, S. Spall strength of shock-loaded glass. *Journal of Applied Physics* **58,** 3249–3251 (1985).

45. Grady, D. E. & Chhabildas, L. *Shock-wave properties of soda-lime glass* tech. rep. (Sandia National Lab.(SNL-NM), Albuquerque, NM (United States), 1996).

46. Dandekar, D. P. Index of refraction and mechanical behavior of soda lime glass under shock and release wave propagations. *Journal of Applied Physics* **84,** 6614–6622 (1998).

47. Rosenberg, Z, Ashuach, Y, Dekel, E & Bar-On, E. The split-target technique for measurements of strength under high shock pressures. *Measurement Science and Technology* **19,** 045706 (2008).

48. Gyftopoulos, E. P. & Beretta, G. P. *Thermodynamics: foundations and applications* (Dover Publications, 2005).

49. Robinson, A. C. *The Mie-Gruneisen Power Equation of State.* tech. rep. (Sandia National Lab.(SNL-NM), Albuquerque, NM (United States), 2019).

50. Saurel, R. & Abgrall, R. A simple method for compressible multifluid flows. *SIAM Journal on Scientific Computing* **21,** 1115–1145 (1999).

51. Mitchell, A. C. & Nellis, W. J. Shock compression of aluminum, copper, and tantalum. *Journal of Applied Physics* **52,** 3363–3374. ISSN: 0021-8979. https://aip.scitation.org/doi/10.1063/1.329160 (2021) (May 1981).

52. MacDonald, R. A. & MacDonald, W. M. Thermodynamic properties of fcc metals at high temperatures. *Physical Review B* **24,** 1715–1724. https://link.aps.org/doi/10.1103/PhysRevB.24.1715 (2021) (Aug. 1981).

53. *AERO-F source code* 2021. https://bitbucket.org/frg/aero-f.

54. *M2C source code* 2022. https://github.com/kevinwgy/m2c.

55. Zaghloul, M. R. Reduced formulation and efficient algorithm for the determination of equilibrium composition and partition functions of ideal and nonideal complex plasma mixtures. *Physical Review E* **69** (2004).

56. Martin, W. *et al. NIST Atomic Spectra Database (version 2.0) (1999)* en. 1999.

57. Alefeld, G., Potra, F. A. & Shi, Y. Algorithm 748: Enclosing zeros of continuous functions. *ACM Transactions on Mathematical Software (TOMS)* **21,** 327–344 (1995).

58. Zaghloul, M. R., Bourham, M. A. & Doster, J. M. A simple formulation and solution strategy of the Saha equation for ideal and nonideal plasmas. *Journal of Physics D: Applied Physics* **33,** 977–984 (2000).

59. Sun, Y., Shi, C., Liu, Z. & Wen, D. Theoretical research progress in high-velocity/hypervelocity impact on semi-infinite targets. *Shock and Vibration* **2015,** 1–15 (2015).